

ASSESSING THE FRICTIONAL AND BAROCLINIC CONTRIBUTIONS
TO STRATIFIED WAKE FORMATION:
A PARAMETER SPACE STUDY

A Thesis

by

JAMIE BROOKE SMITH

Submitted to the Office of Graduate Studies of
Texas A&M University
in partial fulfillment of the requirements for the degree of
MASTER OF SCIENCE

May 2006

Major Subject: Atmospheric Sciences

ASSESSING THE FRICTIONAL AND BAROCLINIC CONTRIBUTIONS
TO STRATIFIED WAKE FORMATION:
A PARAMETER SPACE STUDY

A Thesis

by

JAMIE BROOKE SMITH

Submitted to the Office of Graduate Studies of
Texas A&M University
in partial fulfillment of the requirements for the degree of
MASTER OF SCIENCE

Approved by:

Chair of Committee,	Craig Epifanio
Committee Members,	Fuqing Zhang
	John Nielsen-Gammon
	Robert Hetland
Head of Department,	Richard Orville

May 2006

Major Subject: Atmospheric Sciences

ABSTRACT

Assessing the Frictional and Baroclinic Contributions to Stratified Wake Formation:
A Parameter Space Study.

(May 2006)

Jamie Brooke Smith, B.S., University of California at Davis

Chair of Advisory Committee: Dr. Craig C. Epifanio

The baroclinic and surface-frictional contributions to stratified wake formation are considered as a function of the non-dimensional height ($\epsilon = Nh_o/U$) and aspect-ratio ($\delta = h_o/L$) of the barrier. Numerical simulations are computed for a wide range of the ϵ - δ parameter space, including both unstratified ($\epsilon = 0$) and highly stratified ($\epsilon = 4$) flows and for terrain slopes characteristic of both geophysical ($\delta = 0.1$) and laboratory scale ($\delta = 2.0$) obstacles. Simulations both with and without applied surface stresses are compared to gain insight into the baroclinic and surface-frictional contributions to each flow. Particular emphasis is given to the changes in kinematic wake structure, the relative contributions of skin and pressure drag, and the vertical momentum flux observed as the mountain height and terrain slope are varied. We also examine several cases from the parameter-space study in more detail using a method for decomposing the flow into baroclinic and viscous parts. The decompositions show that for large- ϵ and small- δ flows, wake generation is primarily baroclinic in nature, while at smaller- ϵ and/or larger- δ , the wake becomes increasingly surface frictional.

ACKNOWLEDGEMENTS

I would first like to acknowledge the immense help of my committee chair, Dr. Craig Epifanio, without which I would surely not be where I am right now. Whether explaining the more complicated aspects of the study or simply just humoring my simple questions, his patience and willingness to assist have led me to a degree I would not have reached otherwise. I would also like to thank my additional committee members, Dr. Fuqing Zhang, Dr. John Nielsen-Gammon, and Dr. Robert Hetland for each of their guidance and input. I would also like to thank the Support Staff for all of their assistance with the more bureaucratic part of taking me to this final step. Thanks so much to Pat Price for her ever-patient and kind heart, and whose role as a mother-away-from-home kept me on track and sane here in Aggieland.

More personally, I would like to thank my parents, Doug and Wendy, for their constant support and love throughout my life, pushing me each step closer to becoming a successful and happy person. I would also like to thank my brother, Justin, for making sure I kept things in perspective. Last, I can't express enough how much the love and patience from my fiancé Scott Meier has helped me succeed here at Texas A&M University. With such support, it is no wonder I have made it where I am today.

TABLE OF CONTENTS

	Page
ABSTRACT	iii
ACKNOWLEDGEMENTS	iv
TABLE OF CONTENTS	v
LIST OF FIGURES	vii
 CHAPTER	
I INTRODUCTION	1
a) Towing-Tank Studies	2
b) Mechanisms of Wake Formation	5
c) Objectives	8
II BASIC PHYSICS, SCALE ANALYSIS, AND	
MODEL DESCRIPTION	11
a) Basic Physics and Scale Analysis	11
b) Experimental Design	14
III PARAMETER SPACE RESULTS.....	18
a) Wind-Speed Analysis	18
b) Drag Parameters	25
IV DIAGNOSTIC VORTICITY ANALYSIS	31

CHAPTER	Page
a) Method Overview	31
b) Results for Small Epsilon, Small Delta Flow ($\epsilon = 1.0$).....	34
c) Results for Large Epsilon, Small Delta Flow ($\epsilon = 3.0$).....	37
d) Results for Large Epsilon, Large Delta Flow ($\epsilon = 3.0, \delta = 2.0$)	38
V CONCLUSIONS	41
REFERENCES	44
VITA	47

LIST OF FIGURES

FIGURE	Page
1 TIROS satellite image of two vortices seen from above produced by the wake in the lee of the Canary Islands.....	1
2 Summary diagram depicting features observed in Hawaii's wake.....	3
3 Side and top down view of a wake for homogenous flow ($\epsilon = 0$) with no-slip surface.....	4
4 Side view and top-down view of a wake as for Figure 3 but with $\epsilon = 1.0$	5
5 Side view and top-down view of a wake as for Figure 3 but with $\epsilon = 5.0$	6
6 Streamlines and velocity profiles portraying the frictional mechanism of wake formation.....	7
7 Verification of the dynamic similarity for flows with the same non-dimensional parameters.....	14
8 Regime diagram identifying experiments completed in parameter space.....	16
9 Non-dimensionalized minimum wind speed contour plots.....	19
10 Maximum lee-side buoyancy $b/N^2 h_o$ at the ground at time $15 L/U$ for flows with a) friction, shown with a contour interval of 0.001	

FIGURE	Page
and b) no friction, shown with a contour interval of 0.002.....	20
11 Wake at time $Ut/L = 15$ for $\delta = 2.0$ and: a) $\epsilon = 4.0$ with friction, b) $\epsilon = 4.0$ without friction, c) $\epsilon = 1.0$ with friction, d) $\epsilon = 1.0$ without friction, e) $\epsilon = 0.0$ with friction, and f) $\epsilon = 0.0$ without friction.....	23
12 Wake at time $Ut/L = 15$ for $\delta = 0.1$ and: a) $\epsilon = 4.0$ with friction, b) $\epsilon = 4.0$ without friction, c) $\epsilon = 1.0$ with friction, d) $\epsilon = 1.0$ without friction, e) $\epsilon = 0.0$ with friction, and f) $\epsilon = 0.0$ without friction.....	24
13 Non-dimensionalized pressure drag, skin friction, and total drag shown at time = $15 L/U$	26
14 Momentum flux contour plots for the non-dimensionalized momentum flux for no-slip and free slip flows.....	29
15 Verification of the decomposition and inversion methods for $\delta = 0.4$ and $\epsilon = 3.0$ flow at time = $4 L/U$	35
16 Wind and vorticity fields produced by the decomposition and inversion process for $\epsilon = 1.0$ and $\delta = 0.4$ flow at time = $4 L/U$	36
17 Wind and vorticity fields produced by the decomposition and inversion process for $\epsilon = 3.0$ and $\delta = 0.4$ flow at time = $4 L/U$	37
18 Wind and vorticity fields produced by the decomposition and inversion process for $\epsilon = 3.0$ and $\delta = 2.0$ flow at time = $4 L/U$	39

CHAPTER I

INTRODUCTION

Mesoscale island wakes were first observed in images from the TIROS satellite in the 1960's (Figure 1) downwind of the Madeira and Canary Islands off the west coast of Africa (Hubert and Krueger 1962). Such wakes had not been observed previously because their scale makes them too large to observe directly from the ground but too small to be seen in synoptic data. Even so, subsequent studies have shown that wakes are in fact commonplace features in mountainous regions and occur downstream of a wide variety of topographic obstacles, including both relatively isolated mountains and complex mountain ranges. Lee vortices have also been reproduced repeatedly for research purposes in both towing-tank studies and mesoscale numerical models.



Figure 1. TIROS satellite image of two vortices seen from above produced by the wake in the lee of the Canary Islands. The island is located to the northeast of the figure, and flow is from the top right of the figure to the bottom left. [From Conover 1964 (Their figure 12)]

This thesis follows the style and format of the *Journal of the Atmospheric Sciences*.

The study of atmospheric wake structure has been motivated by a number of practical concerns within the earth sciences. Orographic vortices can recirculate aerosols and pollutants (Figure 2), as has been found with the wake off the island of Hawaii (Smith and Grubišić 1993) and downwind of the Rocky Mountains near Denver (Wilczak and Christian 1989). Lee wakes are also thought to be loosely linked to the initiation and intensification of severe weather, especially in the vicinity of the Denver Cyclone (Wilczak and Christian 1989). Island wakes can impact patterns of biological activity in the lee of the island, as has been demonstrated for the case of Hawaii by Seki et al. (2001). Lastly, PV generation in wakes has been proposed as a key for understanding scale interactions in topographic flows and is thought to play a role in the process of lee cyclogenesis in particular (Aebischer and Schär 1998).

a) Towing-Tank Studies

Much of what we know about the structure of stratified wakes comes from observations of wakes produced in towing-tank experiments, the most well-known of which is the study of uniformly stratified flow past an axisymmetric obstacle conducted by Hunt and Snyder (1980). As discussed in Baines (1995), the topology of the flow patterns observed by Hunt and Snyder depends strongly on the non-dimensional obstacle height (or alternatively the effective stratification) defined by $\epsilon = Nh/U$, where N is the buoyancy frequency, h is the maximum obstacle height, and U is the background

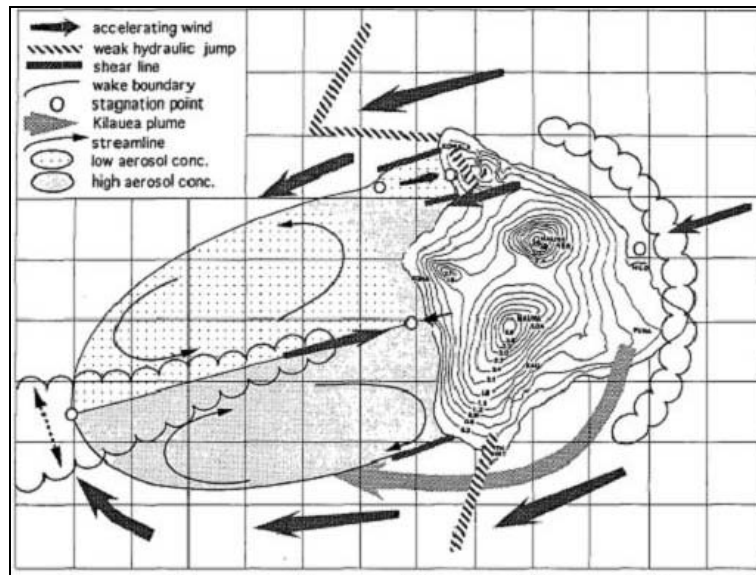


Figure 2. Summary diagram depicting features observed in Hawaii's wake. High aerosol concentration is found in the southern vortex associated with flow past an active volcanic vent on the south side of the island. [From Smith and Grubišić 1993 (Their figure 18)]

wind speed. Further defining the flow is some non-dimensional measure of the width of the barrier, which we take to be the terrain aspect ratio (or slope) defined as $\delta = h/L$ where h is as before and L is the mountain half-width. It should be kept in mind that tank studies typically involve flows past relatively steep obstacles (large δ) and that the results of the Hunt and Snyder study ($\delta \approx 1.5$) may thus differ somewhat from flows past mesoscale topographic obstacles (typically characterized by $\delta \approx 0.1$).

For zero stratification ($\epsilon = 0$), the flow produced by Hunt and Snyder features a horseshoe-like wake pattern with boundary-layer separation first occurring just before the peak of the obstacle (Figure 3). Reversed flow extends to the surface in the lee and as viewed from above the flow takes the form of two counter-rotating vortices. As ϵ increases, the flow above the boundary layer changes in ways consistent with internal

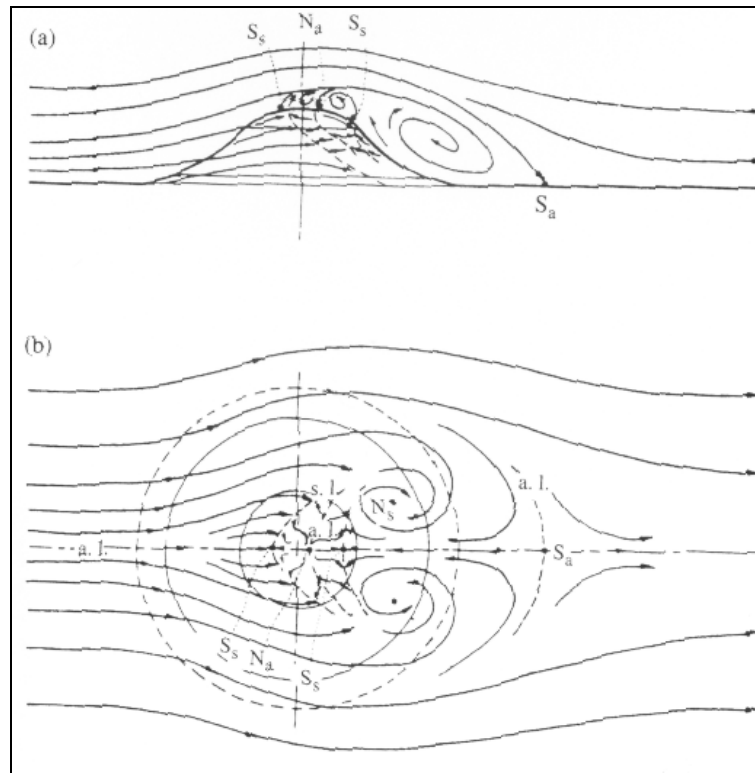


Figure 3. Side and top down view of a wake for homogenous flow ($\epsilon = 0$) with no-slip surface. [Hunt and Snyder (1980) as discussed in Baines (1995) (Baines' figure 6.22)]

wave theory. The separation point moves downstream of the obstacle peak but still exhibits a topology similar to the homogenous case, implying that the kinematic structure of the wake is most likely the same as well (Baines 1995). A particular observation of note is that the wake region becomes progressively more compressed in spatial extent, most likely due to the descending motion in the lee of the obstacle associated with internal wave dynamics aloft. The wake then continues to decrease in intensity as ϵ reaches unity (Figure 4).

Once ϵ becomes somewhat greater than unity, the wake structure begins to change significantly. First, the wake reverses its prior trend and instead begins to

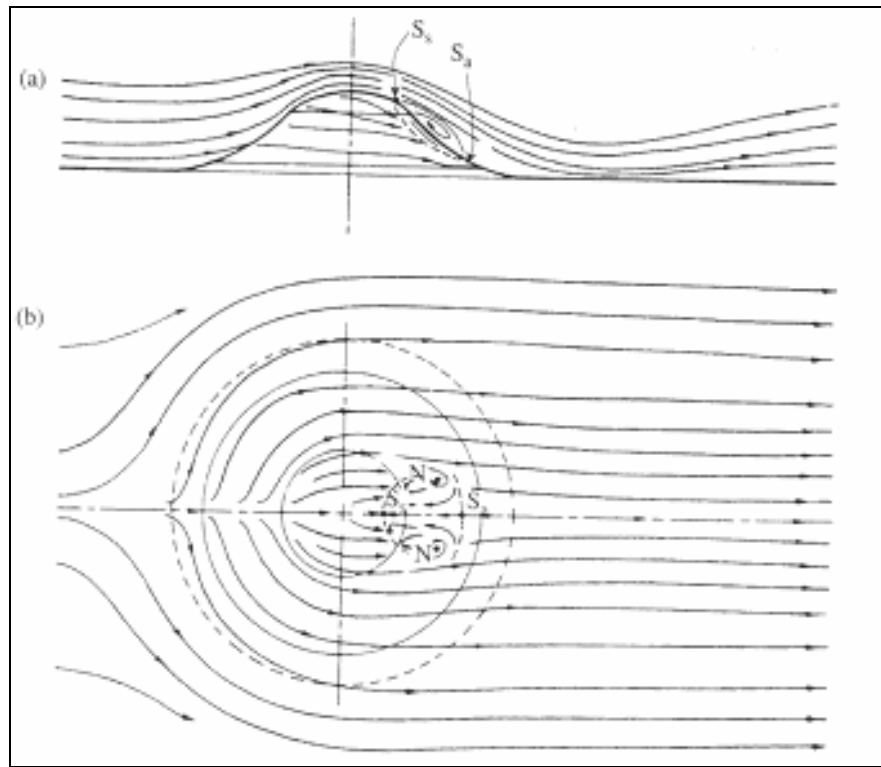


Figure 4. Side view and top-down view of a wake as for Figure 3 but with $\epsilon = 1.0$. [Hunt and Snyder (1980) as discussed in Baines (1995) (Baines' figure 6.25)]

increase rapidly in both intensity and spatial extent as ϵ is made larger (Baines 1995).

The flow also begins to exhibit upstream blocking or “flow-splitting” in which the low-level fluid travels around the obstacle rather than ascending to the peak. These features can be seen in Figure 5.

b) Mechanisms of Wake Formation

While towing-tank studies have provided useful insights into the structure of stratified wakes, they do not directly address the physical mechanism behind wake formation. In principle, there are two potential sources of vorticity in stratified flows: surface friction and interior buoyancy gradients (or baroclinicity). Clearly at $\epsilon = 0$ (as in

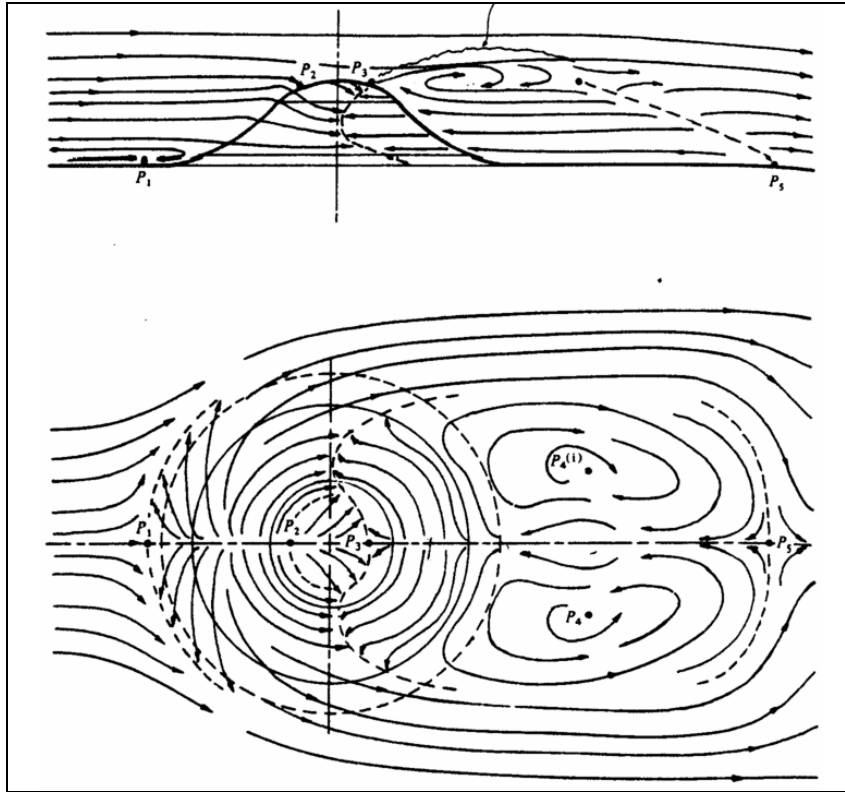


Figure 5. Side view and top-down view of a wake as for Figure 3 but with $\epsilon = 5.0$. [Hunt and Snyder (1980) as discussed in Baines (1995) (Baines' figure 6.26)]

Figure 3) wake formation can only be attributed to the surface frictional mechanism. By contrast, numerical modeling studies have shown that for large ϵ wakes can be produced entirely without surface friction (Smolarkiewicz and Rotunno 1989), in which case the buoyancy gradients in the flow must be responsible for the wake. It is thus apparent that there are two mechanisms leading to wake formation, which we refer to as the frictional and baroclinic mechanisms, respectively.

The frictional mechanism of wake formation has a long history of study in the context of homogeneous flows past bluff bodies (Batchelor 2000 and Kundu and Cohen 2002). Briefly, as the flow encounters an obstacle a boundary layer featuring significant

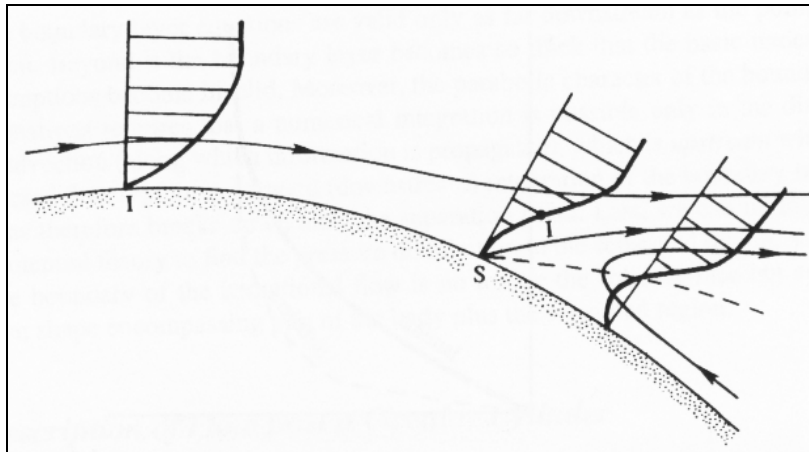


Figure 6. Streamlines and velocity profiles portraying the frictional mechanism of wake formation. “S” is the separation point of the flow, and “I” is the top of the boundary layer. [From Kundu and Cohen 2002 (Their figure 10.12)]

shear vorticity is produced through frictional effects at the obstacle surface. If an adverse pressure gradient forms at the surface then the flow in this boundary layer tends to reverse and the boundary layer then separates from the obstacle as shown in Figure 6. At this point the vorticity in the boundary layer is shed into the fluid interior and a pair of eddies eventually forms such as those seen in Figure 3.

The baroclinic (or more specifically free-slip) process of wake formation has been the subject of extensive theoretical and numerical modeling work over the past one-and-a-half decades (e.g., Smolarkiewicz and Rotunno, 1989; Rotunno and Smolarkiewicz, 1991; Schär and Smith, 1993; Schär and Durran, 1997; Rotunno et al., 1999; Epifanio and Durran, 2002; Schneider et al., 2003; Epifanio and Rotunno, 2005; among others) but nonetheless remains incompletely understood. Schär and Durran (1997) have suggested that wake formation in free-slip flows occurs through one of two processes: the breaking of gravity waves over the lee slope or blocking of the surface flow upstream. For the canonical case of flow with uniform N and U past an axisymmetric obstacle, the

dominant contribution comes from upstream blocking [although breaking waves may also play a role at intermediate ϵ since wave breaking is known to promote upstream blocking and flow deflection (Smith and Grönas, 1993; Epifanio and Durran 2001)]. Epifanio and Rotunno (2005) have shown that blocking in a stratified fluid triggers a lee-side flow response that in many ways resembles the classical retracting piston problem from shallow-water theory. In particular, blocking causes a warm anomaly to form along the lee-slope as potentially warmer air from aloft descends to replace the colder air blocked upstream. The low-level fluid downstream of the barrier is then drawn back into this warm anomaly and inward and thus ultimately ends up streaming along behind the obstacle much like the flow behind a retracting piston.

c) Objectives

Despite the significant body of modeling work on stratified wakes, there has to date been no systematic attempt to compare simulations with and without surface stresses over a broad range of parameter space. Studies that have compared simulations with and without stresses (e.g. Peng and Thompson, 2003; Olafsson and Bougeault, 1997) have mostly been limited to a small range of ϵ (typically $\epsilon > 1$) and a single value of δ (in all cases $\delta \ll 1$). The literature also lacks a study comparing, across ϵ , flows characteristic of both geophysical flows (small δ) and laboratory studies (large δ). Such a comparison is necessary in order to translate characteristics of the flow observed in the laboratory to the geophysical case, given the large difference in terrain slope of the two cases. Based on this need, the objectives of this study are as follows:

1. To characterize the contributions of friction and baroclinicity to wake formation through a direct comparison of numerical simulations both with and without applied surface stresses.
2. To identify regions of the terrain slope/mountain height parameter space in which either surface friction or baroclinicity is the dominant process.
3. To explore changes in
 - a. the kinematic structure of the wake;
 - b. the mechanisms of wake vorticity generation; and
 - c. the relative contributions of form drag and skin drag to the total drag at the surface
 as the mountain height and terrain slope are varied.

The following chapter scales the basic equations for our study and briefly outlines the numerical model and associated experimental design. Chapter III then provides a thorough survey of the mountain height-terrain slope parameter space, with an emphasis on identifying parameter regimes for both the free-slip and applied-surface-stress flow. Some of the flow properties investigated in Chapter III will include the minimum front- and lee-side winds (to assess blocking and wake strength, respectively), the net skin friction and pressure drags. Chapter IV provides a detailed look at several cases from the parameter-space study using the Lagrangian vorticity decomposition method outlined by Epifanio and Durran (2002). The frictional and baroclinic parts of the vorticity as well as

the associated induced flow fields are computed in an effort to better understand the processes leading to wake formation in each case.

CHAPTER II

BASIC PHYSICS, SCALE ANALYSIS AND MODEL DESCRIPTION

The objectives outlined in the previous chapter are addressed through a series of modeling experiments using the numerical model described by Epifanio and Durran (2001) and Epifanio (2006). Here we review the basic physics of our problem and provide a brief overview of our numerical model and experimental design. Particular emphasis is given to determining the key parameters that provide the basis for our parameter space study.

a) Basic Physics and Scale Analysis

The model used for this study is based on the compressible Boussinesq equations given by

$$(1) \quad \frac{D\mathbf{u}}{Dt} = -\nabla P + b\hat{\mathbf{k}} - \nabla \cdot \mathbf{T}$$

$$(2) \quad \frac{Db}{Dt} + N^2 w = -\nabla \cdot \mathbf{B}$$

$$(3) \quad \frac{\partial P}{\partial t} + c_s^2 \nabla \cdot \mathbf{u} = 0$$

with kinematic lower boundary condition

$$(4) \quad w = \mathbf{u} \cdot \nabla h \quad \text{at} \quad z = h$$

Here P is the Boussinesq disturbance pressure, b is the buoyancy, \mathbf{T} is the stress tensor, \mathbf{B} is the diffusive heat flux, N is the basic-state buoyancy frequency and c_s is the constant Boussinesq sound speed (see Appendix C of Epifanio and Rotunno (2005) for a

discussion of the compressible Boussinesq system). In all experiments we let the undisturbed background state be described by constant N and U . The Boussinesq potential temperature variable can then be written $\Theta = N^2 z + b$ and the stress tensor \mathbf{T} and diffusive heat flux \mathbf{B} are defined as

$$(5) \quad T_{ij} = -K \left(\frac{\partial u_i}{\partial x_j} + \frac{\partial u_j}{\partial x_i} - \frac{2}{3} \delta_{ij} \nabla \cdot \mathbf{u} \right)$$

$$(6) \quad B_j = -K \frac{\partial b}{\partial x_j}$$

Here the kinematic viscosity K is the sum of a constant background value K_0 and a turbulent eddy viscosity K_e . The lower boundary conditions on \mathbf{T} and \mathbf{B} are the surface-stress and thermal insulation conditions defined by

$$(7) \quad T_{ij} n_j s_i = -C_d \mathbf{u} \cdot \hat{s} |\mathbf{u}|$$

$$(8) \quad T_{ij} n_j t_i = -C_d \mathbf{u} \cdot \hat{t} |\mathbf{u}|$$

$$(9) \quad B_j n_j = 0$$

where \hat{n} is the unit normal to the terrain, \hat{s} and \hat{t} are the unit tangents in the xz and yz planes, respectively (and where the standard summation convention applies to repeated indices), and C_d is the drag coefficient. The spatial and temporal scales of the wakes of interest are too small to be significantly affected by the Coriolis force, so it is neglected.

In order to analyze the flow, the key control parameters must be identified. We begin by determining the appropriate scales. Given that no one set of disturbance scales will accurately describe the flow for all flow regimes in this study, we instead opt for a relatively generic set of scaling parameters by letting the disturbance length and depth scales be determined by the topography and letting the disturbance wind scale be set as

U. As such, we assume appropriate scales for fluctuation length, depth, and time to be $(x, y) \sim L$, $z \sim h_o$, and $t \sim L/U$. The horizontal velocities (both fluctuation and total magnitude) are assumed to scale as $(u, v) \sim U$. Using these scales in the lower boundary condition then gives $w \sim Uh_o/L$, which further implies $b \sim N^2 h_o$. The horizontal momentum equations give us the pressure scale $P \sim U^2$. With these scales, our full set of non-dimensional variables is then defined as

$$\begin{aligned}
 (x, y) &= L(\hat{x}, \hat{y}) & z &= h_o \hat{z} & t &= L/U \hat{t} \\
 (10) \quad (u, v) &= U(\hat{u}, \hat{v}) & w &= Uh_o/L \hat{w} & h &= h_o \hat{h} \\
 b &= N^2 h_o \hat{b} & P &= U^2 \hat{p}
 \end{aligned}$$

Substituting (10) into the set of equations (1) through (9) yields four non-dimensional control parameters. The first two, the non-dimensional mountain height ϵ and the terrain slope δ , are as defined in the introduction. The Reynolds number, a measure of the background viscosity of the system, is defined by

$$(11) \quad R_e = \frac{UL}{K_o} \delta^2$$

where K_o is the background kinematic viscosity. The fourth parameter is the non-dimensional surface drag, defined by

$$(12) \quad \mu = \frac{c_o U h_o}{K_o}$$

where c_o is the maximum value of C_d . Note that while these four parameter definitions will not necessarily reflect the sizes of various terms in the governing equations under all

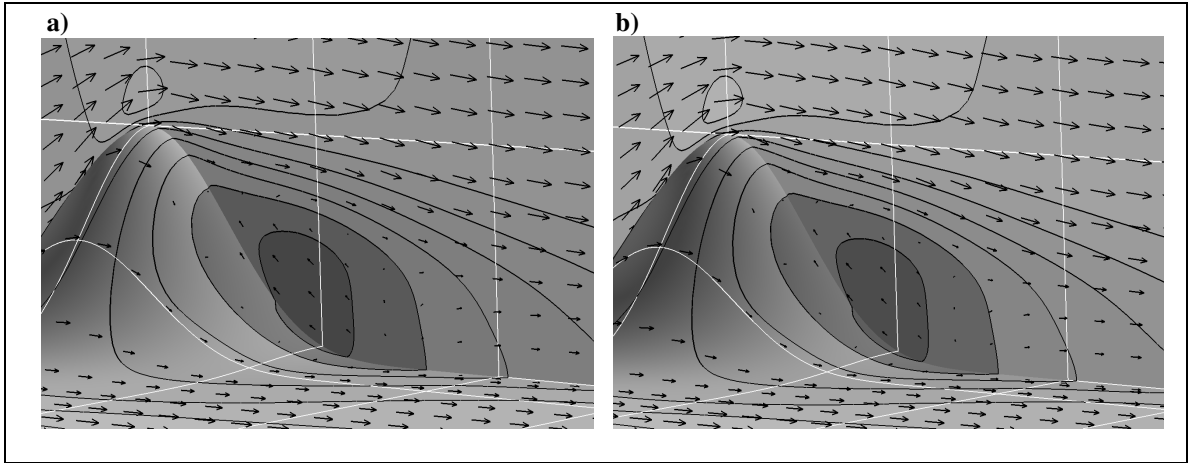


Figure 7. Verification of the dynamic similarity for flows with the same non-dimensional parameters. The shading shows the cross-ridge wind component u/U (contour interval equal to 2 ms^{-1}) while the vectors show the velocity \underline{u}/U . Results are shown in both the centerline plane $y = 0$ and at the obstacle surface. Grid lines show horizontal distance in units of $2L$ and vertical distance in units of h_o . In both panels the non-dimensional control parameters for the flow are $\epsilon = 0.0$, $\delta = 1.0$, $R_e = 400$ and $\mu = 12$, but the dimensional values of h_o , L , and K_o differ by a factor of two between the experiments.

flow regimes, they do guarantee dynamic similarity so as to uniquely define the flow in a non-dimensional sense, as illustrated in Figure 7.

b) Experimental Design

As previously mentioned, the model we will use to perform our experiments is essentially that developed by Epifanio and Durran (2001), with some modifications to address surface friction. The modifications follow the work of Epifanio (2006) and allow the surface stresses to be implemented correctly under steep-slope conditions (rather than relying upon the flat-boundary approximation as is currently typical in mesoscale models). The model is non-hydrostatic and compressible Boussinesq, and handles acoustic propagation through the split-time-step algorithm introduced by Klemp and Wilhelmson (1978). The terrain is incorporated through use of the terrain-following

coordinate transformation of Gal-Chen and Sommerfield (1975). The turbulent eddy viscosity K_e is defined through the subgrid-scale turbulence parameterization of Lilly (1962), and the surface stresses are defined using the standard roughness-length parameterization based on similarity theory.

The obstacle shape used in this study is described by the following

$$(13) \quad h(x, y) = \begin{cases} \frac{h_0}{16} [1 + \cos(\pi \frac{r}{4L})]^4, & \text{if } r = (x^2 + y^2)^{1/2} < 4L; \\ 0, & \text{otherwise,} \end{cases}$$

where which describes a bell-shaped obstacle of half-width L that decays to zero over a distance of $4L$. The domain size in x and y is $20L \times 20L$ and the terrain is centered at $9L \times 10L$. The horizontal grid spacing is set at $0.08L$. The vertical grid spacing at the surface is held at 25 meters (or $0.025h_0$), small enough to resolve the shear layer at the boundary at even the steepest mountain height. For model efficiency, a geometric stretching factor of 1.02 increases the vertical grid spacing with height, so that the highest vertical resolution is achieved in the lowest layers of the grid where the majority of the wake response is found. The vertical domain depth is chosen as the greater of $6\pi U/N$ or $2.5L$ for cases with $N \neq 0$ and $2.5L$ for the $N = 0$ case. This ensures at least three waves in the vertical for the stratified cases as well as sufficient room for the potential-flow response at $\epsilon = 0$. To prevent reflection of waves a portion of the domain below the upper boundary is dedicated to a sponge layer with depth (D_s) determined by $D_s = (D_T - h_0)/2$, where D_T is height of the model lid. The model is initialized from potential flow in order to mimic an impulsive start (Rotunno and Smolarkiewicz, 1991).

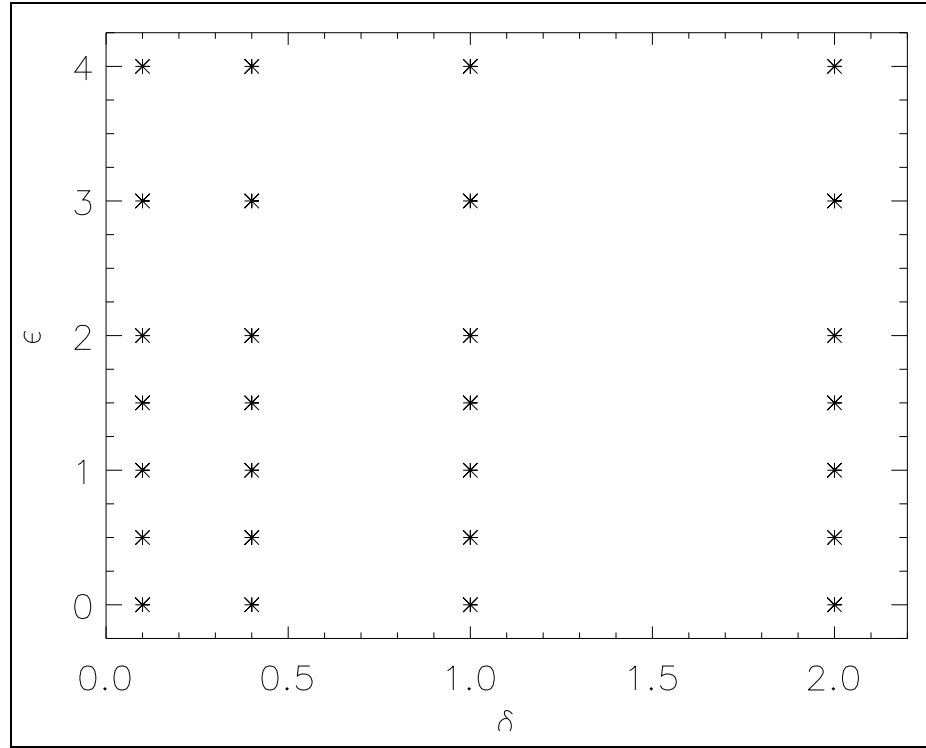


Figure 8. Regime diagram identifying experiments completed in parameter space (indicated by an asterisk (*)). Each ϵ - δ combination is run both with ($\mu = 12$) and without ($\mu = 0$) applied surface stresses.

In mapping out parameter space, the mountain height h_o and background wind U are held constant in all experiments so that ϵ is varied through changes in static stability. Representative values have been chosen with ϵ ranging from 0 to 4 (Figure 8). Since h_o is held fixed at 1 km, δ is varied by changing L . The mountain half-width varies from 500 meters to 10 km, with δ ranging from 0.1 to 2.0. Each of the runs across the ϵ and δ parameter space is computed using both surface friction ($\mu = 12$) and free-slip ($\mu = 0$) conditions. For runs with surface friction the roughness length is specified so that the non-dimensional drag parameter μ is given by $\mu = 12$. This value was found to produce results qualitatively similar to those of Hunt and Snyder (1980) at large δ (as seen in the following chapter). On the other end of the spectrum, $\mu = 12$ corresponds to a roughness

length of 0.0168 for our $\delta = 0.1$ cases, characteristic of a surface covered with long grass (Oke, 1978). The Reynolds number is held fixed at 400.

CHAPTER III

PARAMETER SPACE RESULTS

Here we present a survey of the ϵ - δ parameter space for simulations both with and without applied surface stresses. This chapter provides the context for the diagnostic computations presented in Chapter IV. This section is also interesting in its own right, as the large- δ parameter space has not been mapped in previous studies.

The specific flow properties studied in this section include the minimum front and lee-side wind, maximum lee-side buoyancy, pressure drag and skin friction. All results in this chapter are presented for time $15 L/U$. At this time the flow is quasi-stationary and has not yet been corrupted by lateral boundary reflections observed at later times.

a) Wind-Speed Analysis

The strength of the lee-side wake is measured in terms of the minimum x-component of wind (u) along the centerline plane downwind of the peak. This minimum value is taken between the surface and the fifth vertical grid level. This allows the wind above the shear layer to be measured in the cases with surface friction but at the same time avoids the potential for ambiguity associated with deceleration in the mountain wave aloft. For our purposes, we let a wake be defined as a flow with negative minimum lee-side value of u . That is, we use the term wake to refer to a lee-side flow structure with

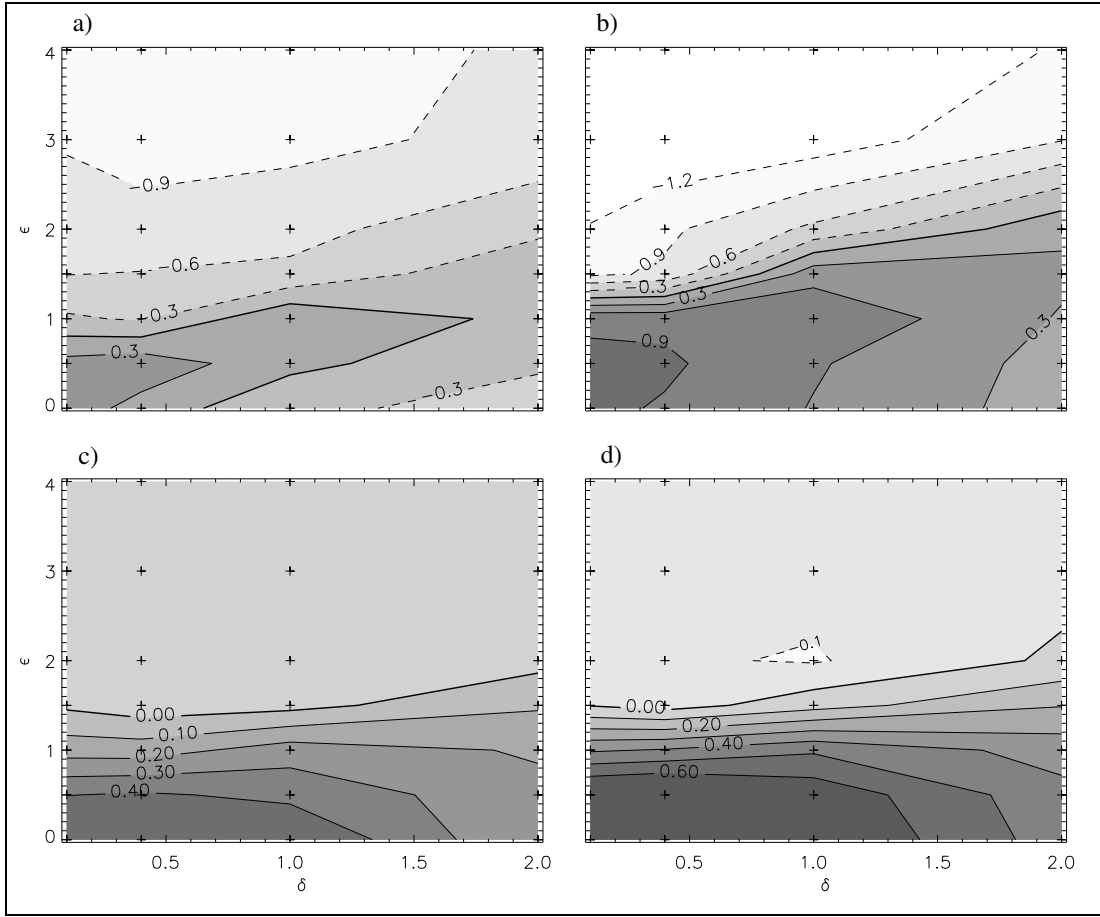


Figure 9. Non-dimensionalized minimum wind speed contour plots. Shown are minimum u/U in the lee for a) no-slip flows and b) free-slip flows, shown with a contour interval of 0.3, and minimum wind speed on the front for c) no-slip flows and d) free-slip flows with a contour interval of 0.1. For all plots, δ is shown on the x-axis, ϵ is shown on the y-axis, and shading becomes darker as values increase. $\epsilon - \delta$ pairs corresponding to our numerical simulations are shown with + signs.

return flow and recirculating eddies.

Figure 9b shows the minimum lee-side u as a function of ϵ and δ for the free-slip case ($\mu = 0$). As expected, wake formation in the free-slip case is observed only for flows at large ϵ . For future reference we refer to this large- ϵ region of reversed lee-side flow as regime I, while the small- ϵ region without reversed flow is regime II. Note that the transition between these two regimes with increasing ϵ has distinct

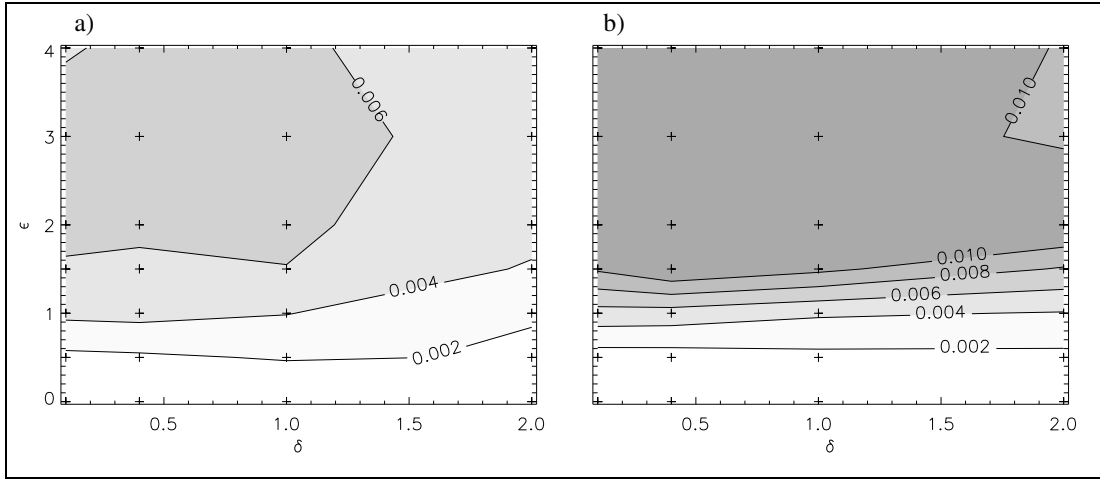


Figure 10. Maximum lee-side buoyancy $b/N^2 h_o$ at the ground at time $15 L/U$ for flows with a) friction, shown with a contour interval of 0.001 and b) no friction, shown with a contour interval of 0.002. For all plots, δ is shown on the x-axis, ϵ is shown on the y-axis, and shading becomes darker as values increase. Plus signs are as described in Figure 9.

δ dependence, with larger values of ϵ needed to produce a wake at large δ . The abruptness of the transition also appears to vary with δ , with a particularly abrupt transition observed on the small- δ end of the spectrum.

Figure 9d shows the minimum surface value of u along the centerline plane upstream of the peak. By definition, a minimum upstream value of u less than zero indicates that the upstream flow is blocked. Comparison of Figures 9b and 9d shows that in the free-slip calculations the occurrence of upstream blocking is nearly coincident with the onset of lee-side flow reversal. (Indeed, all of our free-slip flows with wakes also exhibit upstream blocking.) This correlation between blocking and lee-side flow reversal suggests that the mechanism of wake formation in the free-slip case is likely that discussed by Epifanio and Rotunno (2005). In this scenario, blocking causes a warm anomaly to form along the lee slope which then drives wake formation, similar to the effect of a retracting piston in shallow water theory. Consistent with this theory is the

maximum lee-side buoyancy seen in Figure 10b. Note that the strongest ϵ -gradient in buoyancy is found at roughly the same ϵ where blocking occurs.

Comparison of Figures 9 a and c with Figures 9 b and d shows that the parameter-space dependence for the simulations with surface stresses exhibits many similarities to that observed for the free-slip case. The first observation of note is that both cases show a similar wake regime at large ϵ (regime I). The fact that this wake regime is present in similar form under both experimental conditions suggests that the wake in regime I is likely baroclinically driven. Also similar to the frictionless regime is that as δ increases, the transition to this large ϵ wake regime occurs at larger ϵ . Lastly, the onset of blocking, seen in Figure 9c, remains essentially unchanged with the addition of friction.

The most obvious difference between the free-slip and no-slip cases in Figure 9 is the presence of an additional wake regime at small ϵ in the no-slip case (hereafter regime III). Because this wake regime is absent in the free-slip cases (at least within the range of δ addressed), it is likely driven by frictional effects. Figure 9a shows that the occurrence of such a small- ϵ wake is strongly dependent on δ , with larger δ implying a greater tendency towards wake formation. This δ dependence of wake formation is consistent with the results of previous laboratory studies for small- ϵ flows (see review in Baines (1995), section 5.1).

Another notable difference between the free-slip and surface-stress runs is that the strength of the wake in regime I for the applied stress cases is decreased when compared to regime I in the free-slip runs. This indicates that friction may be hindering the wake

rather than helping it under these conditions. Lastly, the transition from no wake to wake with increasing ϵ in Figure 9a is no longer coincident with blocking as it was for the free-slip cases. As seen in Figures 9a and 9b, the no-slip Region I wake occurs before the onset of blocking, and there is no correlation to maximum buoyancy (Figure 10a) as there was for free-slip conditions. This occurrence of a wake prior to blocking suggests that the frictional mechanism adds enough vorticity to the flow that blocking is no longer a prerequisite for the formation of reversed flow.

A qualitative comparison between free-slip and surface-stress flows is shown in Figure 11 for the case $\delta = 2.0$. Consistent with Figure 9d, the free-slip case forms a wake only at large epsilon ($\epsilon = 4.0$ case shown in Figure 11f). By contrast, a wake is present in the frictional case for all ϵ . Note that the ϵ -dependence of the surface friction case is qualitatively very similar to that observed in the laboratory by Hunt and Snyder (1980). In particular an increase in ϵ from zero to unity is accompanied by a marked reduction in the strength of the wake (as in Figures 3 and 4). For larger ϵ the trend reverses and the wake rapidly intensifies (as in Figure 5).

Figure 12 shows a similar comparison between free-slip and no-slip runs for the case $\delta = 0.1$. In contrast to the $\delta = 2.0$ case, neither the free-slip nor the surface-stress flow shows a wake for $\epsilon = 0$. For $\epsilon = 1.0$ a wake occurs only in the surface-stress flow. The presence of a wake under no-slip conditions for $\epsilon = 1$ is notable, as blocking has not yet occurred for this case. Mechanisms for the formation of this wake will be explored

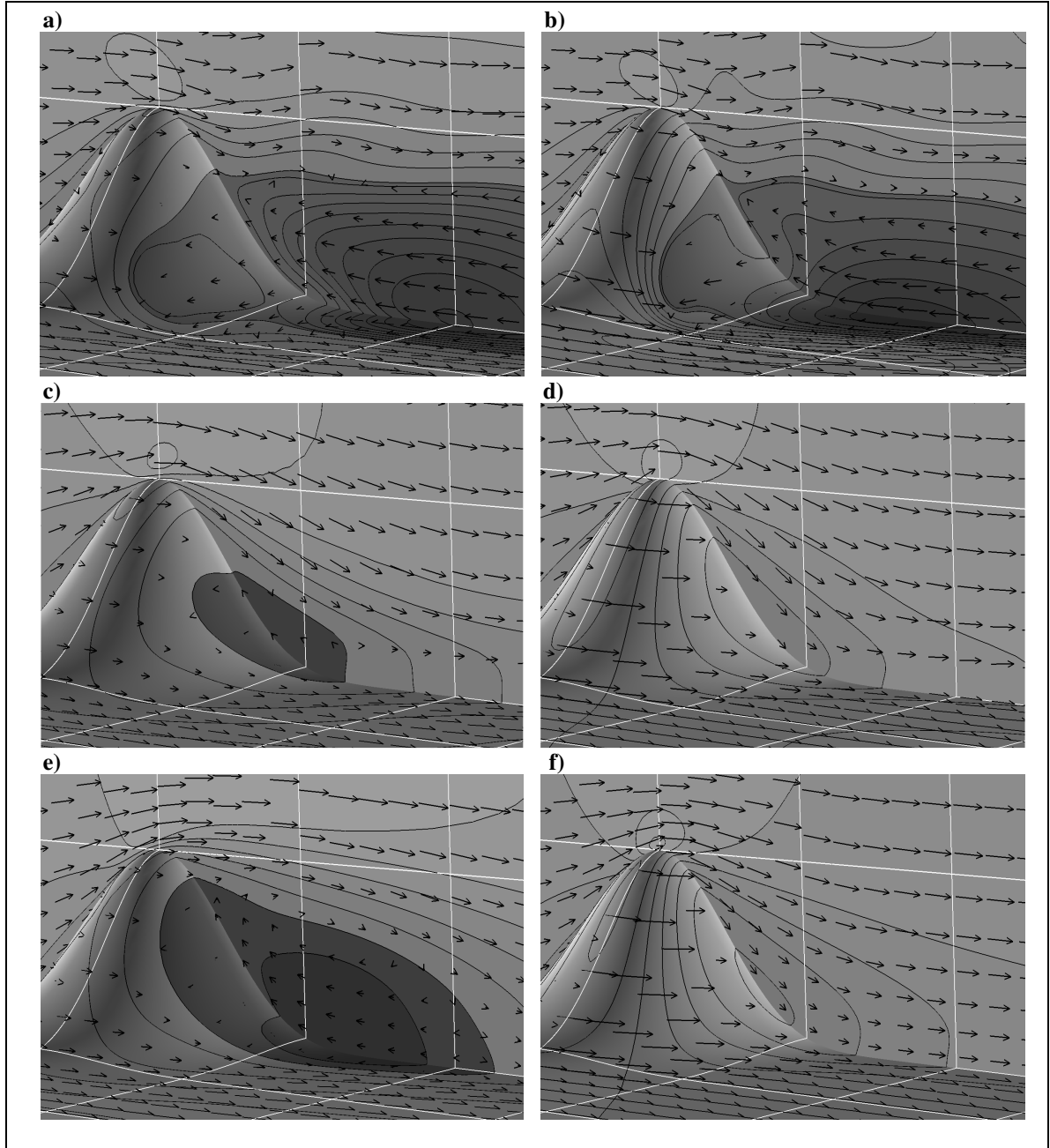


Figure 11. Wake at time $Ut/L = 15$ for $\delta = 2.0$ and: a) $\epsilon = 4.0$ with friction, b) $\epsilon = 4.0$ without friction, c) $\epsilon = 1.0$ with friction, d) $\epsilon = 1.0$ without friction, e) $\epsilon = 0.0$ with friction, and f) $\epsilon = 0.0$ without friction. Shown are u/U and the wind vector \underline{u}/U both in the centerline plane $y = 0$ and at the terrain surface. Dark grey tones represent negative values of u , while light grey tones represent positive values, with a contour interval of 0.2. Grid lines show horizontal distance in units of $2L$ and vertical distance in units of h_o ,

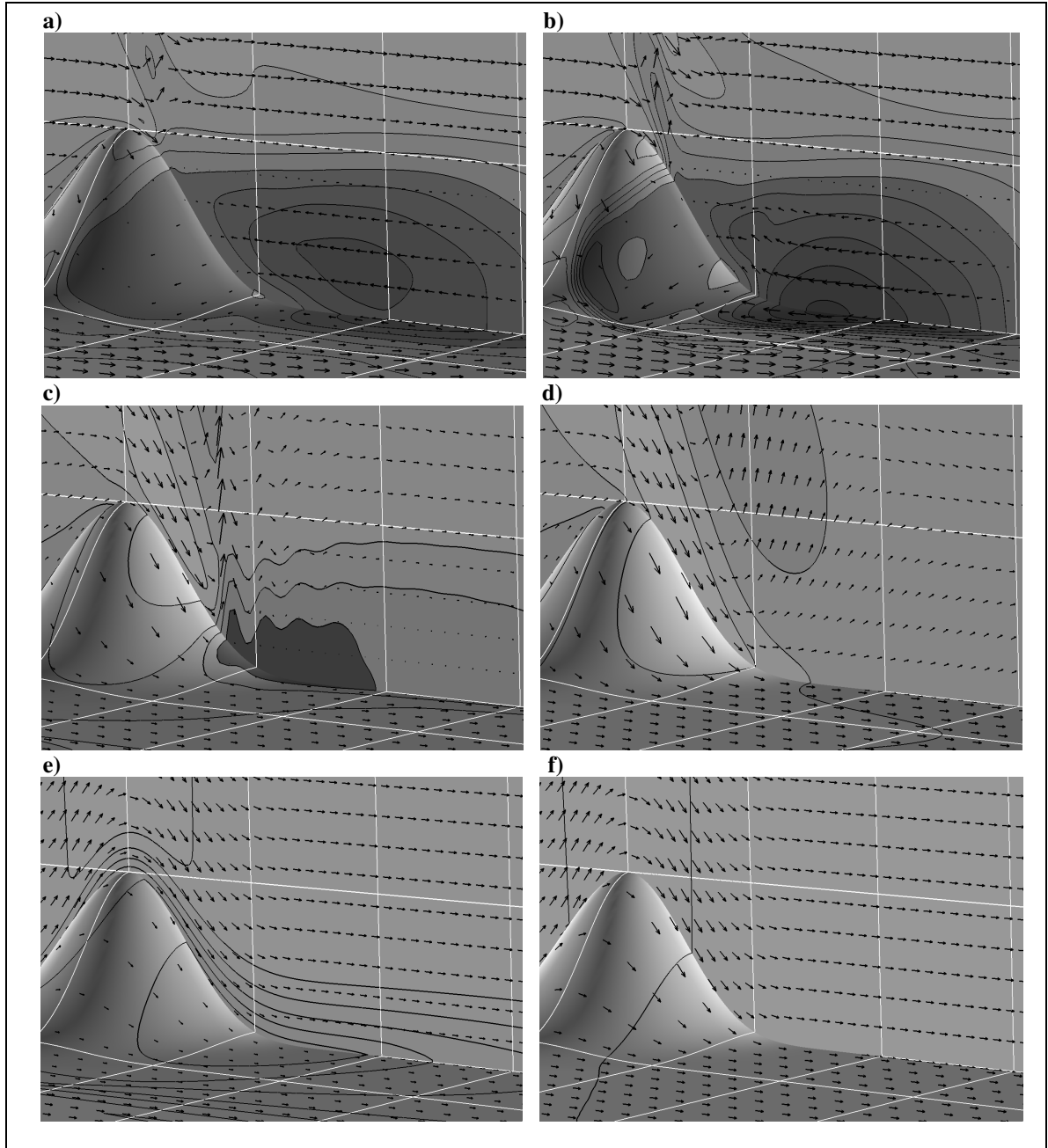


Figure 12. Wake at time $Ut/L = 15$ for $\delta = 0.1$ and: a) $\epsilon = 4.0$ with friction, b) $\epsilon = 4.0$ without friction, c) $\epsilon = 1.0$ with friction, d) $\epsilon = 1.0$ without friction, e) $\epsilon = 0.0$ with friction, and f) $\epsilon = 0.0$ without friction. Shown are u/U and the wind vector \underline{u}/U both in the centerline plane $y = 0$ and at the terrain surface. Dark grey tones represent negative values of u , while light grey tones represent positive values. Panels (a) and (b) present a contour interval of 0.1 while for the remaining panels the contour interval is 0.3. Grid lines show horizontal distance in units of $2L$ and vertical distance in units of h_o ,

further in Chapter IV. Also a notable difference when compared to the $\delta = 2.0$ flows is the stronger mountain wave signature at small delta. While this wave signature has little direct effect on the wake itself, it affects the flow structure close to the obstacle peak and implies a transfer of momentum to higher altitudes.

b) Drag Parameters

The drag associated with mountains constitutes a significant sink term in the global atmospheric momentum budget. This topographic drag takes two forms: the pressure drag associated with the net pressure difference across the barrier and the skin friction due to the net viscous transport across the boundary. Part of the drag is in general carried away by mountain waves, while the rest is realized locally in the wake. Here we consider the pressure drag and skin friction as functions of epsilon and delta for our simulations both with and without applied surface stresses.

The pressure drag (D_p) is defined as the x-component of the pressure force exerted by the fluid on the boundary, i.e.,

$$(14) \quad D_p = \iint p \frac{\partial h}{\partial x} dx dy = u^2 h_0 L \hat{D}_p$$

Physically, the skin friction (D_{sf}) is the net viscous transport of u across the boundary over the entire domain. This is non-dimensionalized by

$$(15) \quad D_{sf} = \iint \tau_{1j} \eta_j \sqrt{1 + \left(\frac{\partial h}{\partial x}\right)^2 + \left(\frac{\partial h}{\partial y}\right)^2} dx dy \sim K_o \frac{U}{h_o} L^2 \hat{D}_{sf}$$

This non-dimensionalization is misleading though, because it assumes that the shear layer depth scales as h_o , when in reality it should scale as h_o/R_e . In the following we scale both

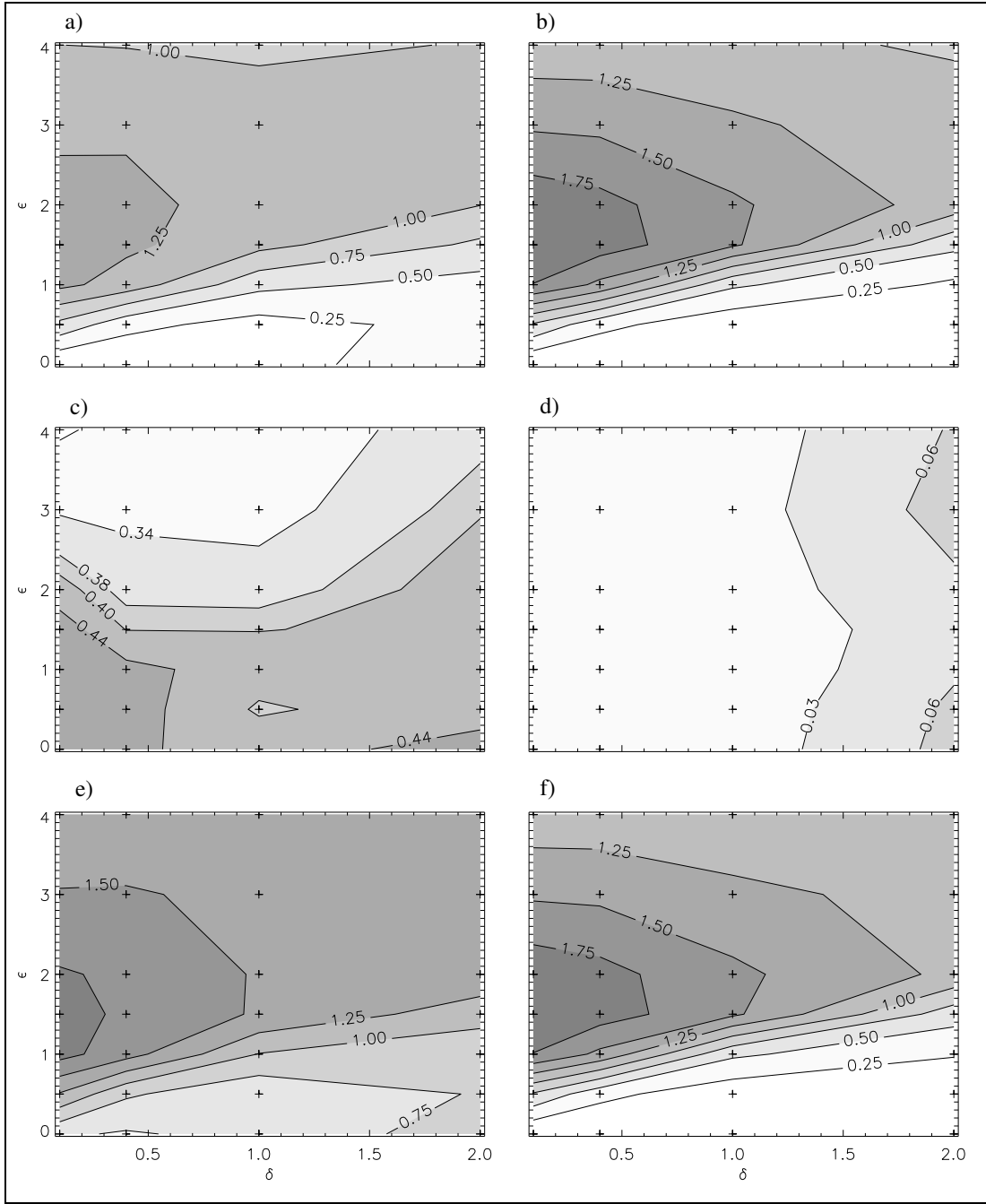


Figure 13. Non-dimensionalized pressure drag, skin friction, and total drag shown at time = $15 L/U$. Pressure drag is shown for a) no-slip flow and b) free-slip flows, with a contour interval of 0.25. Skin friction is shown for c) no-slip flow and d) free-slip flows, with a contour interval of 0.03. Last, the total drag is shown for e) no-slip flow and f) free-slip flow with a contour interval of 0.25. For all plots, δ is shown on the x-axis, ϵ is shown on the y-axis, and shading becomes darker as values increase. Plus signs indicate model runs performed.

pressure drag and skin friction by $U^2 h_o L$ so as to allow direct comparison between the two types of drag.

Figure 13 shows the pressure drag (13 a and b), the skin friction (13 c and d), and the sum of the two (13 e and f) for the no-slip and free-slip flows, respectively. First examining the free-slip case (Figure 13b), we notice that the pressure drag increases rapidly as the mountain height approaches the critical value for the onset of lee-side flow reversal (cf. Figure 9b). This increase in drag is most likely associated amplification of the internal wave response aloft. By comparison the drag in the wake regime remains relatively uniform in ϵ . The drag generally increases with decreasing δ and exhibits a maximum at intermediate ϵ and small δ . Lastly, the skin friction is negligible, but shows a slight increase with δ .

Comparison of Figures 13a and 13b shows that for most of the $\epsilon - \delta$ parameter space the addition of surface friction leads to a significant reduction in pressure drag. Even so, the general pattern of the drag is qualitatively similar in the two cases, suggesting that for most of the parameter space the pressure drag is governed primarily by baroclinic processes. The main exception to this result is again the wake regime at large- δ and small- ϵ , where the addition of surface friction leads to a local area of increased drag missing in the free-slip cases. Note that while surface stresses cause a reduction in pressure drag over most of the parameter space, adding in the skin friction results in a total drag that is greater than the free-slip case at small ϵ and comparable to the free-slip case in the large- ϵ wake regime (cf. Figures 13e and 13f).

The last parameter relating to the drag is the momentum flux, which measures the downward transport of momentum by mountain waves as averaged over a specified horizontal surface; i.e.,

$$(16) \quad M = \iint u w dx dy = U^2 h_o L \hat{M}$$

where for the present calculations the integration domain is the surface $z = 1.1h_o$. The momentum flux thus measures the part of the total topographically induced drag that is carried away by mountain waves and thus realized aloft rather than below the terrain peak.

The momentum flux shows a maximum at small δ and intermediate ϵ under conditions both with and without friction. This is the area of parameter space most strongly affected by mountain waves and is also nearly coincident with the maximum pressure drag seen in Figure 13. Note that the momentum flux increases with decreasing δ in both the wave and wake regimes. In all case the momentum flux is reduced in the simulations with surface friction, but the difference between the free-slip and surface-stress cases is greatest at small δ and diminishes as δ increases.

The ratio of momentum flux to the pressure drag (Panels c and d) shows that mountain waves carry a higher percentage of the drag created by the topography under small δ intermediate ϵ conditions. (The peak seen in the free-slip case (Figure 14d) at small δ and small ϵ is a result of an extremely low value of pressure drag for that flow, without which the contour plot would be similar in nature to that for no-slip.) For the intermediate- ϵ case at $\delta = 0.1$, nearly 90% of the pressure drag is carried away by

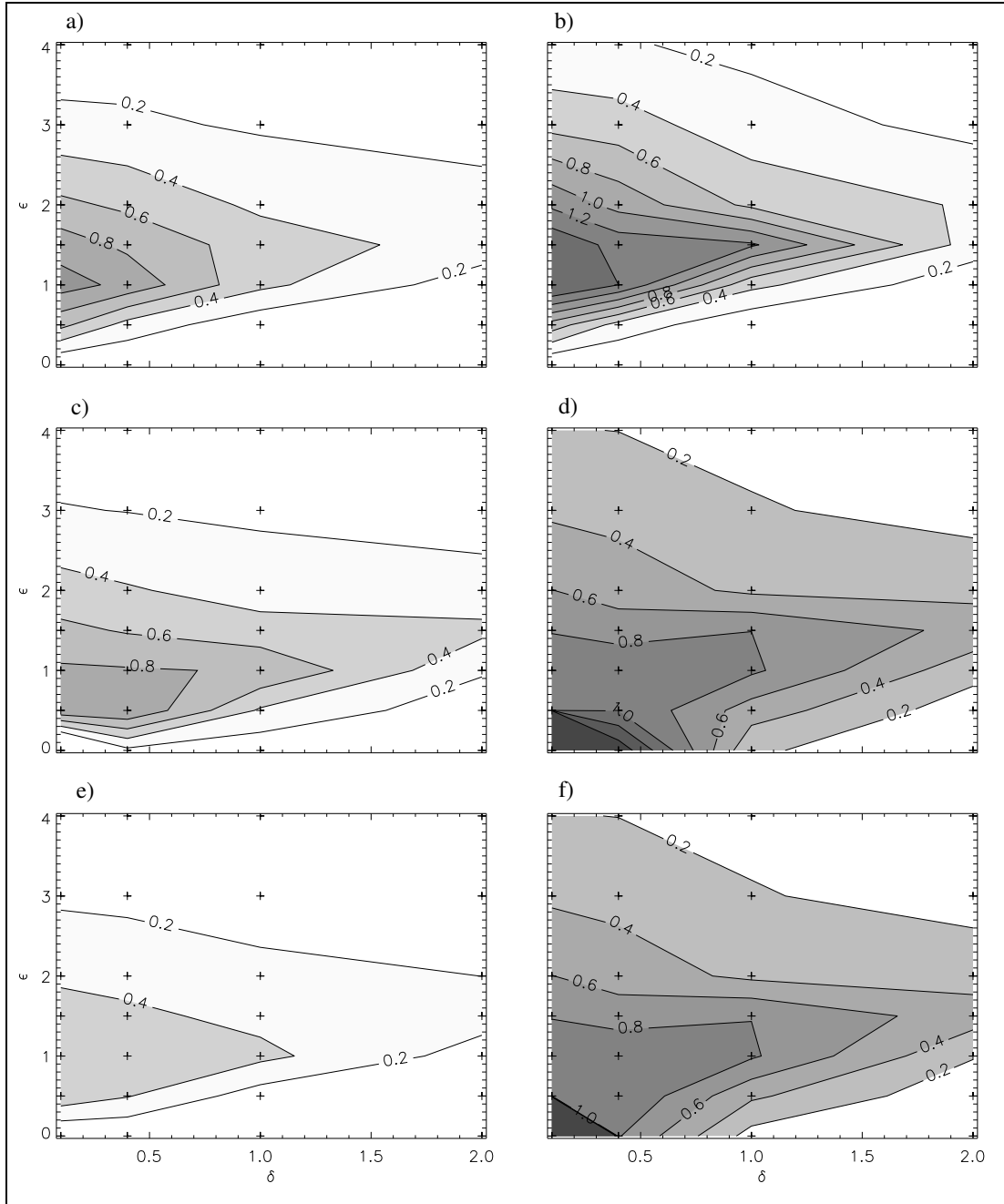


Figure 14. Momentum flux contour plots for the non-dimensionalized momentum flux for a) no-slip and b) free slip flows. Also shown are the ratio of momentum flux to pressure drag for c) no-slip and d) free-slip flows, and the ratio of momentum flux to the total drag for e) no-slip and f) free-slip flows. For all panels, a contour interval of 0.2 is shown, with darker shades of grey indicating larger values. Plus signs indicate model runs performed

mountain waves in both the free-slip and surface-stress cases. However, this percentage is significantly lower throughout most of the large- ϵ wake regime. Note in particular that for $\epsilon = 4.0$ the percentage drops below 20% for most of the range of δ studied.

Figure 14e shows that if we consider the drag due to skin friction as well, then less than half of the total topographic drag is carried away by mountain waves even in the regime of maximum momentum flux. This compares to nearly 90% of the total drag for the free-slip case (Figure 14f).

CHAPTER IV

DIAGNOSTIC VORTICITY ANALYSIS

The results of Chapter III show that for some regions of $\epsilon - \delta$ parameter space wakes occur only in runs with surface friction, while in other cases wakes are found in the free-slip case as well. Furthermore, in cases with free-slip wakes the addition of friction almost always causes a corresponding reduction in the strength of reversed flow in the wake. A tentative interpretation of these results is then that wakes that occur only in runs with surface friction are primarily frictional in origin, while wakes that occur in both free-slip and surface-stress runs are primarily baroclinic.

In the present chapter we test this basic assumption for surface friction wakes by applying a method for decomposing the vorticity and associated flow fields into baroclinic and viscous parts. We begin by providing a brief overview of the method—more detailed presentations developed from a Lagrangian perspective can be found in both Epifanio and Durran (2002) and Davies-Jones (2006). We then apply the method to several examples from the parameter-space study in an effort to diagnose the associated baroclinic and viscous parts.

a) Method Overview

Assuming incompressibility the curl of (1) yields the 3-D vorticity equation

$$(17) \quad \frac{D\boldsymbol{\zeta}}{Dt} = (\boldsymbol{\zeta} \cdot \nabla)\mathbf{u} - \mathbf{k} \times \nabla b + \nabla \times \mathbf{F}$$

where $\zeta = (\xi, \eta, \zeta)$ is the total vorticity, \mathbf{k} is the unit vector in the vertical direction, and $\mathbf{F} = -\nabla \cdot \mathbf{T}$ is the viscous force per unit mass vector (\mathbf{T} is as defined in Chapter II). From a practical standpoint, the decomposition method then amounts to integrating (17) separately for each of the baroclinic and viscous source terms while allowing the full flow field \mathbf{u} to stretch and tilt the vorticity thus generated. As such, the baroclinic vorticity ζ^B satisfies

$$(18) \quad \frac{D\zeta^B}{Dt} = (\zeta^B \cdot \nabla)\mathbf{u} - \mathbf{k} \times \nabla b$$

while the viscous part ζ^V is given by

$$(19) \quad \frac{D\zeta^V}{Dt} = (\zeta^V \cdot \nabla)\mathbf{u} + \nabla \times \mathbf{F}$$

Here \mathbf{u} , \mathbf{F} , and b are determined diagnostically from the integration of (1) – (3) and can thus be taken to be known functions of space and time. From the standpoint of the decomposition method the vorticity equation (16) is then a linear function of ζ , thus guaranteeing that $\zeta = \zeta^B + \zeta^V$.

In flows with surface friction the application of boundary conditions constitutes a significant source of vorticity for the flow. For the diagnostic calculations we apply the boundary conditions for vorticity in two steps. We first note that (18) is essentially an inviscid equation (since $\nabla \times \mathbf{F}$ is neglected) and can therefore be integrated directly at the boundary to obtain $\zeta^B(z = h)$. The boundary condition for the viscous vorticity is then obtained by subtracting ζ^B from the total; i.e.

$$(20) \quad \zeta^V(z = h) = \zeta(z = h) - \zeta^B(z = h)$$

where $\zeta(z = h)$ is computed diagnostically from the model integration of (1) – (3).

Once the separate vorticity fields ζ^B and ζ^V have been computed, we then invert each part separately to obtain associated flow fields using the 3-D inversion algorithm outlined by Epifanio and Rotunno (2005) and Hirasaki and Hellums (1970). The inversion method involves first decomposing the flow into irrotational and vortical parts as

$$(21) \quad \mathbf{u} = \nabla\varphi + \nabla \times \boldsymbol{\psi}$$

where φ is the scalar potential, defining the irrotational part of the flow, and $\boldsymbol{\psi}$ is the vector potential, defining the vortical part of the flow. The irrotational flow in this context is defined to be the standard potential flow past the obstacle, and serves as the initial state for the model simulations. The vortical part then describes the disturbance from the initial state and is defined by

$$(22) \quad \begin{aligned} \nabla^2 \boldsymbol{\psi} &= -\boldsymbol{\zeta} & \text{with both} \\ \nabla \cdot \boldsymbol{\psi} &= 0 & \text{and} \quad \boldsymbol{\psi} \times \hat{n} = 0 \end{aligned}$$

along the boundary. As in the flow decomposition, the inversion process is linear so that we can solve equation (21) separately for ζ^B and ζ^V and add to obtain

$$(23) \quad \begin{aligned} \mathbf{u} &= \nabla\varphi + \nabla \times \boldsymbol{\psi}^B + \nabla \times \boldsymbol{\psi}^V \\ &= \nabla\varphi + \mathbf{u}^B + \mathbf{u}^V \end{aligned}$$

where \mathbf{u}^B and \mathbf{u}^V are then the baroclinic and viscous parts of the flow, respectively.

The separation into viscous and baroclinic parts is most naturally applied in the context of a vorticity-vector potential model, in which case the decomposition (23) will hold identically. In a pressure-velocity model, however, the decomposition will in general

not hold exactly due to inconsistencies in the numerical approximations to (1) and (16). To improve the accuracy of the decompositions we have computed all simulations in this section with a reduced horizontal grid spacing of $\Delta x = \Delta y = 0.05 L$ and with a vertical grid spacing of $\Delta z = 0.0124 h_o$ at the lower boundary (stretched as described in Chapter II). As the simulations are shown at early times only, we have also decreased the horizontal domain size to $14 L \times 14 L$ with the mountain centered at $x = 6 L$ and $y = 7 L$. All physical parameters for the simulations (including the roughness length and reference height for the stress parameterization) are identical to those described in Chapter II.

Figure 15 shows a verification of the decomposition algorithm for the case of $\epsilon = 3.0$ and $\delta = 0.4$ at time $Ut/L = 4$. The left hand-side panels show the total wind and vorticity as taken from the model simulations while the right hand-side panels show the corresponding sums of the baroclinic and viscous parts as determined by the diagnostic vorticity and inversion computations. We note that the case shown in Figure 15 proved the most difficult decomposition to compute. The accuracy of the other decompositions in this chapter is thus comparable to or better than that shown in Figure 15. In all cases the accuracy of the decompositions became less acceptable after time $Ut/L = 4$, and we therefore limit our attention to the results at this time.

b) Results for Small Epsilon, Small Delta Flow ($\epsilon = 1.0$)

We first performed the vorticity decomposition and subsequent inversion for flow with $\delta = 0.4$ and $\epsilon = 1.0$. This case is particularly interesting as it occurs in an area of parameter space where the wake with surface friction occurs prior to blocking. In

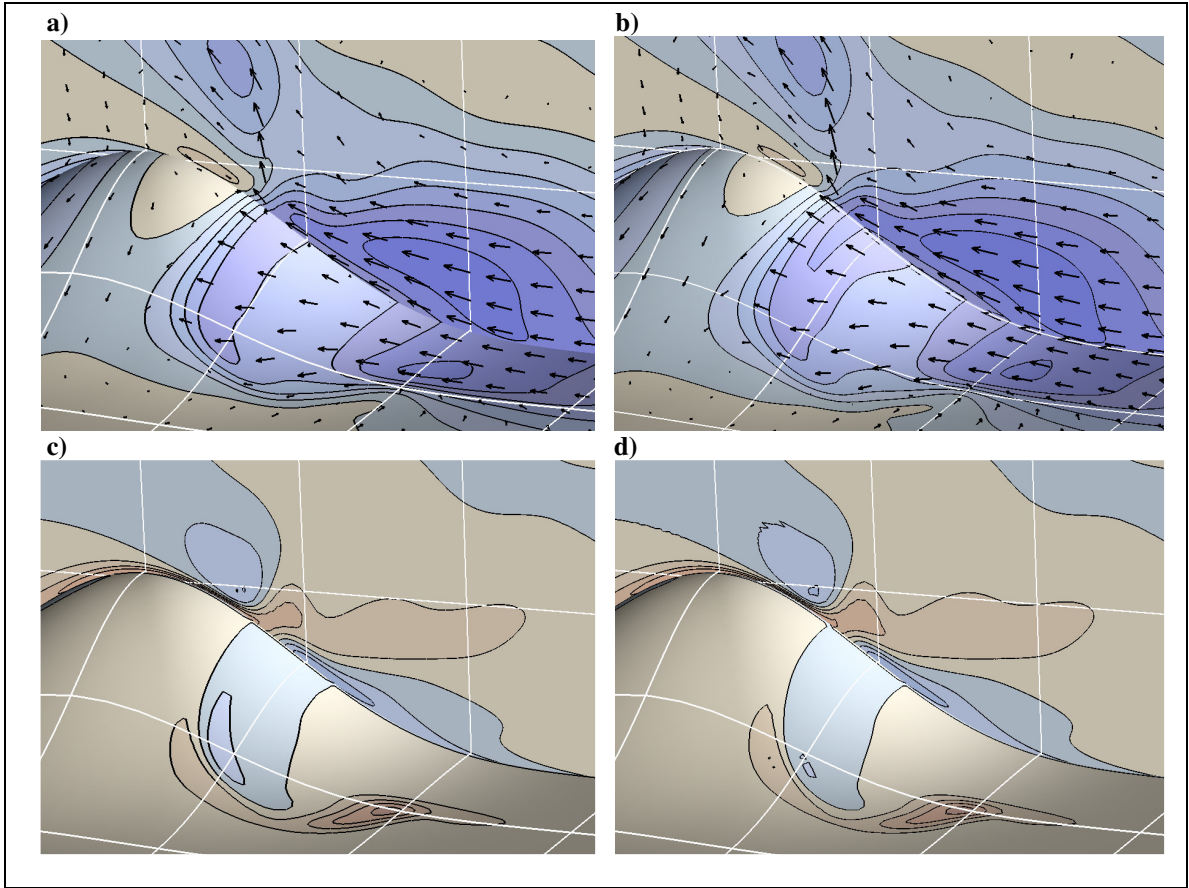


Figure 15. Verification of the decomposition and inversion methods for $\delta = 0.4$ and $\epsilon = 3.0$ flow at time $= 4 L/U$. The top two panels show a) the wind field produced by the model and b) the sum of the baroclinic and viscous wind fields from the decomposition and inversion. Each is shown with the vortical part of u/U shaded with a contour interval of 0.2 and the vortical velocity denoted by vectors. The bottom two panels show c) the vorticity field taken from the model and d) the sum of the baroclinic and viscous vorticity fields produced by the decomposition and inversion. These are shown with $h_0\eta/U$ on the cross-section and the non-dimensional component of vorticity normal to the ground, each with a contour interval of 2.0. For all panels, blue tones represent negative values while orange tones represent positive values.

addition, while a wake occurs in the flow with surface stress it is absent in the free-slip case. At the time of the diagnostic calculations, the wake is not far developed as flow reversal occurs at $3.6 L/U$.

The decomposition and inversion process for this flow produced the wind and vorticity fields shown in Figure 16. The viscous wind field, seen in Figure 16b, shows an area of reversed flow towards the base of the obstacle indicative of wake formation. This

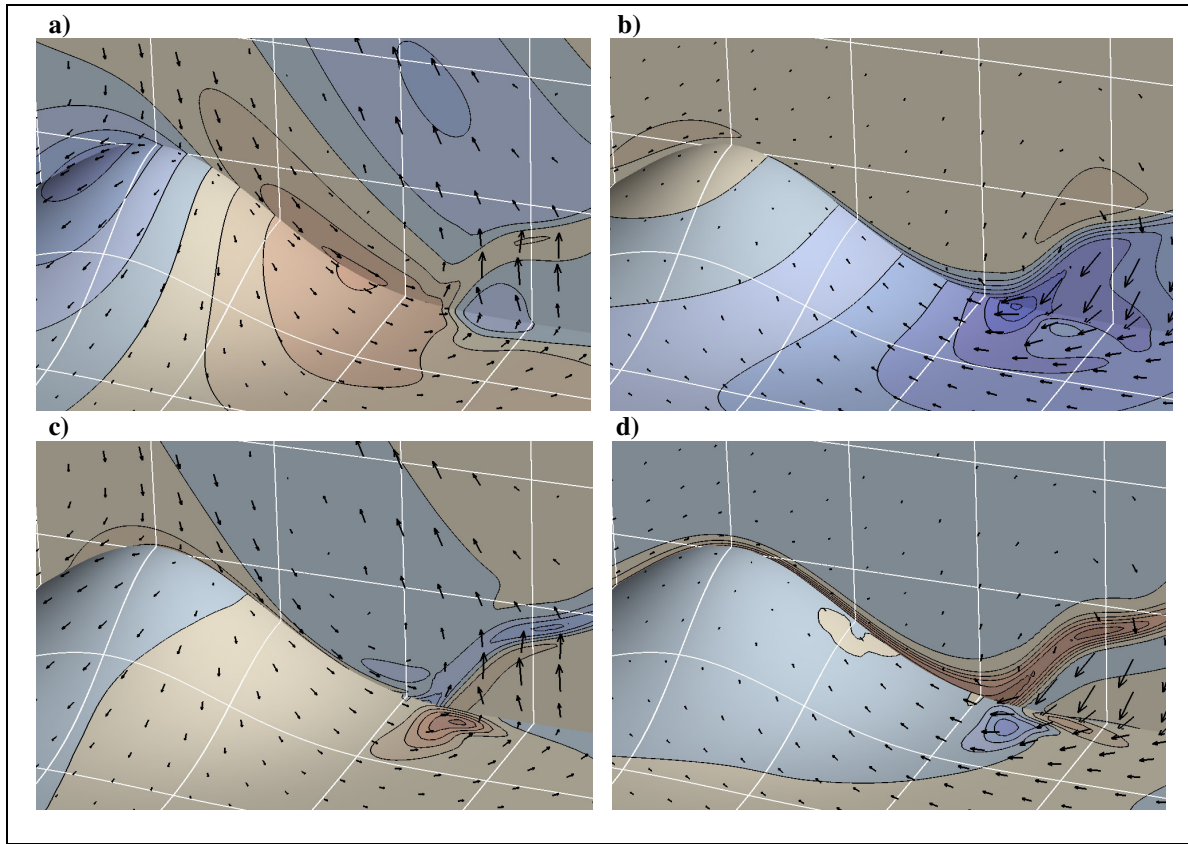


Figure 16. Wind and vorticity fields produced by the decomposition and inversion process for $\epsilon = 1.0$ flow at $\delta = 0.4$ at time $= 4 L/U$. The a) baroclinic and b) viscous parts of u/U are each shown with a contour interval of 0.2 with the corresponding velocities plotted as vectors. The c) baroclinic and d) viscous vorticity fields are shown with non-dimensional contour interval of 1.0 for the y-component of vorticity along the centerline plane, and 0.75 for the terrain normal vorticity at the ground. For all panels, orange shading denotes positive values, while blue shading denotes negative values.

reversed flow is associated with strong positive y-component of vorticity in the centerline plane (Figure 16d) produced by separation of the boundary layer. A small area of positive terrain-normal vorticity is also present at the surface. The baroclinic wind and vorticity fields show a different story, with a more significant area of positive terrain normal vorticity at the boundary seen in Figure 16c. However, the surface winds show little tendency towards flow reversal in the wake (Figure 16a). (Note that flow reversal in this case is primarily driven by the y-component of vorticity, as the terrain normal component

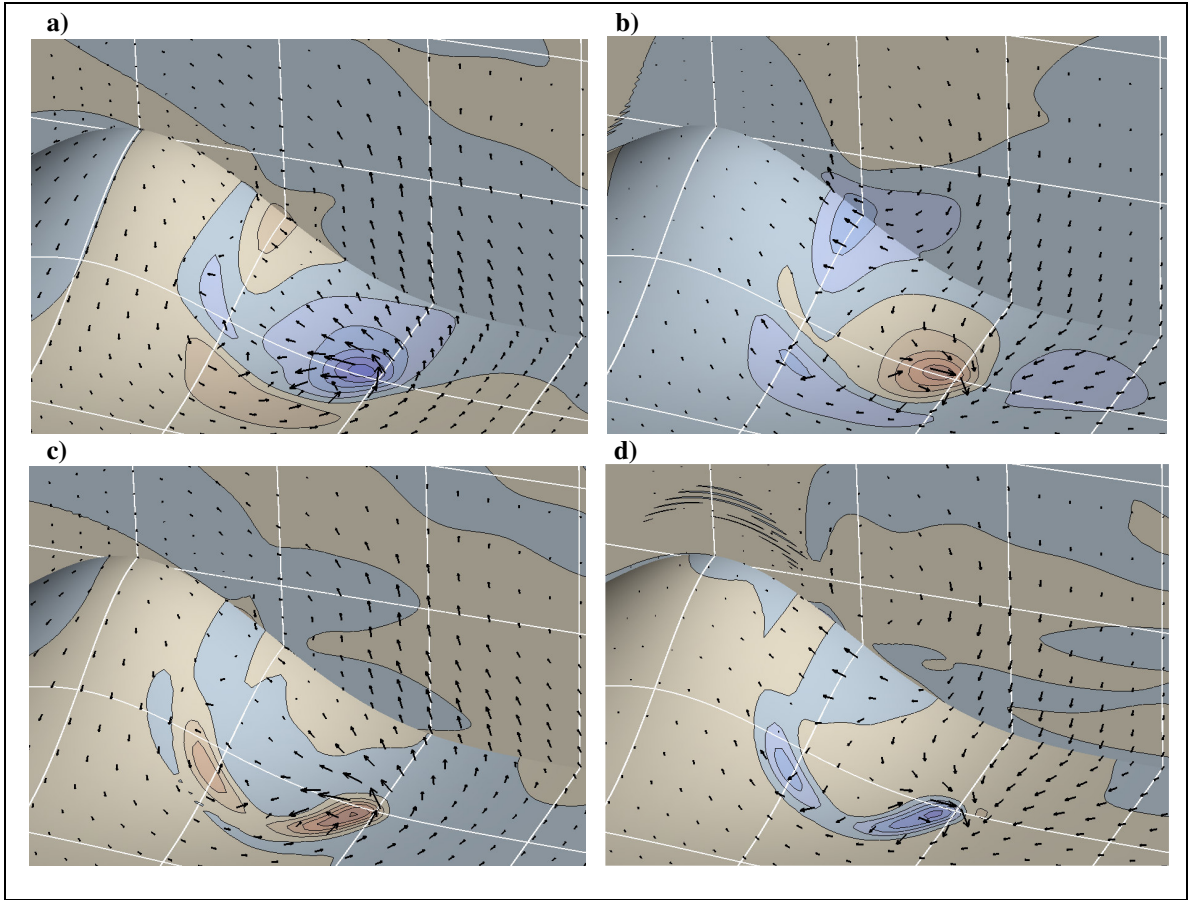


Figure 17. Wind and vorticity fields produced by the decomposition and inversion process for $\epsilon = 3.0$ flow at $\delta = 0.4$ at time $= 4 L/U$. The a) baroclinic and b) viscous parts of u/U are each shown with a contour interval of 1.0 with the corresponding velocities plotted as vectors. The c) baroclinic and d) viscous vorticity fields are shown with non-dimensional contour interval of 10.0 for the y-component of vorticity along the centerline plane, and 5.5 for the terrain normal vorticity at the ground. For all panels, orange shading denotes positive values, while blue shading denotes negative values.

is a factor of three smaller.) We can thus conclude that the wake for this case is primarily frictionally driven, but with minor baroclinic contributions.

c) Results for Large Epsilon, Small Delta Flow ($\epsilon = 3.0$)

To analyze the contributions of the baroclinic and viscous terms to large epsilon wake formation with blocking (see Figure 9c), we examine the $\delta = 0.4$ and $\epsilon = 3.0$ flow with surface friction. We expect this wake to be dominated by baroclinicity, as results

from the previous chapter show similar wakes present in both the surface frictional and free-slip cases. In this instance, flow reversal occurs at $0.86 L/U$, so the wake at the time of the diagnostic calculations is more mature than in the previous case.

Figure 17 shows the baroclinically and viscous produced winds and vorticity for this large epsilon flow. It is immediately apparent that this is primarily a baroclinically produced wake, as Figure 17a shows a region with strongly reversed flow and cyclonic rotation at the base of the terrain in the baroclinic wind field. This cyclonic rotation is associated with an area of positive terrain-normal vorticity at the surface (Figure 17c). The viscous contribution to the wind field (Figure 17b) shows the previously suggested tendency for friction to hinder the wake at the surface in this region of parameter space. The vorticity also supports this, as there is an area of negative terrain-normal vorticity at the ground. Note that while the frictionally produced wind acts as a drag in the body of the wake, there is an area of reversed flow approximately half-way up the mountain seen solely in the viscous wind field (Figure 17b) near the location of the separation point for the flow. As such, we can thus conclude that while the flow near the separation point is determined by the viscous contribution to vorticity, the wake overall is primarily baroclinically driven.

d) Results for Large Epsilon, Large Delta Flow ($\epsilon = 3.0$, $\delta = 2.0$)

The parameter space study of the previous chapter suggests an increased frictional contribution to wake formation at large δ . To analyze the effect of increased terrain slope on the baroclinic and viscous terms of vorticity at large ϵ , we examine the $\delta = 2.0$ and

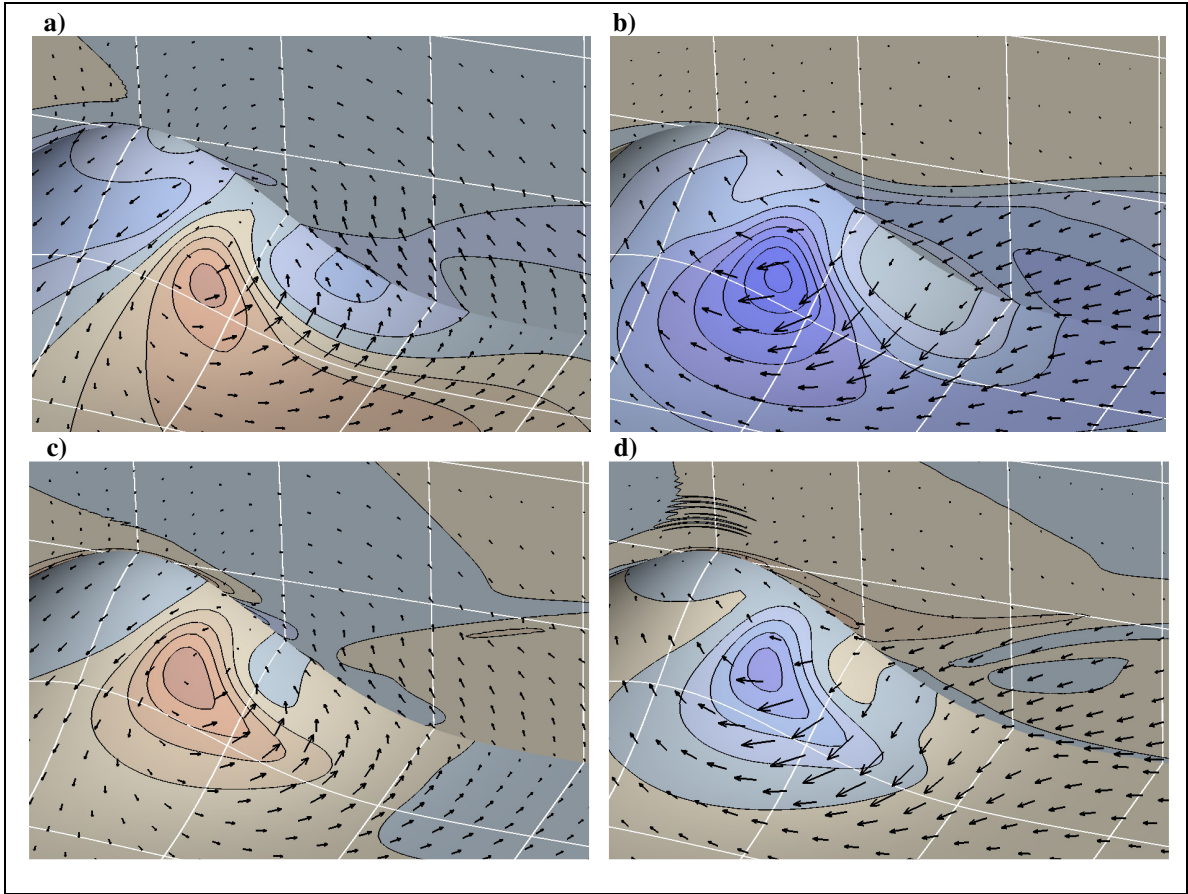


Figure 18. Wind and vorticity fields produced by the decomposition and inversion process for $\epsilon = 3.0$ flow at $\delta = 2.0$ at time $= 4 L/U$. The a) baroclinic and b) viscous parts of u/U are each shown with a contour interval of 0.25 with the corresponding velocities plotted as vectors. The c) baroclinic and d) viscous vorticity fields are shown with a non-dimensional contour interval of 4.0 for the y-component of vorticity along the centerline plane, and 7.5 for the terrain normal vorticity at the ground. For all panels, orange shading denotes positive values, while blue shading denotes negative values.

$\epsilon = 3.0$ flow with surface friction. This case again has wake formation with blocking, as well as a wake in the free-slip case. Here, flow reversal occurs at time $1.1 L/U$.

This case proves to be more ambiguous than the previous two. We see significant flow deceleration in the viscous wind field (Figure 18b), but little cyclonic rotation in the wind vectors. The terrain-normal vorticity (Figure 18d) is also negative over the lee slope and only weakly positive further downstream. On the other hand, the baroclinically-

produced winds (Figure 18a) show significantly less reversed flow in the wake but do show cyclonic rotation in the wind vectors. The baroclinic vorticity shows this as well, with an area of strongly positive terrain normal vorticity over the lee slope. These results suggest that both mechanisms of wake formation play a role, with the viscous component driving flow reversal and baroclinicity contributing rotation.

CHAPTER V

CONCLUSIONS

The baroclinic and frictional contributions towards wake formation have been examined as they relate to flow past a bell-shaped obstacle. A parameter space study was completed examining changes in the flow properties as the non-dimensional mountain height ϵ and the non-dimensional terrain slope δ were varied. Simulations both with and without applied surface stresses were compared in an effort to gain insight into the relative contributions of friction and baroclinicity.

An examination of the minimum lee side wind shows the presence of a wake with reversed flow at large mountain height under both free-slip and surface-frictional conditions. For this area of parameter space, surface friction is found to reduce the reversed flow in the wake relative to the free-slip case, implying that the wake is likely baroclinically driven and even hindered by surface friction. A second wake region is present at large- δ and small- ϵ only in the surface frictional runs, indicating a frictionally driven wake. Minimum front-side winds show a strong correlation between blocking and lee-side reversed flow for the free-slip case, as the blocking curve is nearly coincident with the transition to reversed flow in the lee. This correlation breaks down under no-slip conditions, where a lee-side wake is found prior to blocking.

The contributions of viscosity and baroclinicity towards wake formation were examined in more detail by applying a method to decompose the flow into baroclinic and viscous parts. The method involves integrating the vorticity equation twice, once with

only the baroclinic source term, and once with only the viscous term. The results of this decomposition are then inverted separately to obtain baroclinic and viscous flow fields.

We first examined a case at $\epsilon = 1.0$ and $\delta = 0.4$, in order to examine why a wake forms prior to the onset of blocking in the no-slip case. The results for this case show a strong area of reversed flow in the viscous wind field, indicative of a frictionally produced wake. By comparison, the baroclinically-produced reversed flow is weak. We then examined the $\epsilon = 3.0$ and $\delta = 0.4$ case, where the wake forms in the presence of blocking. The baroclinic wind field for this case shows strong cyclonic rotation in the wake, while the viscous wind field acts opposite to this everywhere except near the separation point along the lee-slope. This indicates a primarily baroclinically-produced wake, with friction only playing a role near the separation point. For our final case we examined flow at $\epsilon = 3.0$ and $\delta = 2.0$ to identify the effect of increasing the terrain slope. The vortical wind field for this case shows significant deceleration along the lee slope but no cyclonic rotation. By comparison, the baroclinic wind field shows only weak reversed flow but does contribute cyclonic rotation to the wake. This indicates that both mechanisms play a role in wake formation, with viscosity dominating flow reversal and baroclinicity inducing the rotation.

In addition to examining wake formation, our parameter space study also considered the pressure drag and momentum flux produced by the obstacle as a function of ϵ and δ . As expected, each of these quantities shows a maximum in the mountain wave regime at intermediate- ϵ and small- δ . Comparing the flows with surface friction to those without shows a marked decrease in both pressure drag and momentum flux in the runs

with surface friction. However, adding the skin friction increases the total drag to values comparable in both the free-slip and surface frictional runs. Looking at the ratio of momentum flux to total drag, we see greater than 80% of the total momentum transported up by mountain waves in the free-slip case, which is reduced to less than 50% for the frictional case.

REFERENCES

- Aebischer, U. and Schär, C., 1998: Low-Level Potential Vorticity and Cyclogenesis to the Lee of the Alps. *J. Atmos. Sci.*, **55**, 186–207.
- Baines, P.G., 1995: *Topographic Effects in Stratified Flows*. Cambridge University Press, 482 pp.
- Batchelor, G. K., 2000: *An Introduction to Fluid Dynamics*. Cambridge University Press, 635 pp.
- Kundu, P. K., and I. M. Cohen, 2002: *Fluid Mechanics*. Academic Press, 700 pp.
- Conover, J.H., 1964: The Identification and Significance of Orographically Induced Clouds Observed by TIROS Satellites. *J. of Appl. Meteor.*, **3**, 226-234.
- Davies-Jones, Robert, 2006: Integrals of the Vorticity Equation. Part I: General Three- and Two-Dimensional Flows, *J. Atmos. Sci.* (in press)
- Epifanio, C.C., 2006: A Method for Imposing Surface Stress and Heat Flux Conditions in Finite Difference Models With Steep Terrain. *Mon. Wea. Rev.* (in preparation)
- , C. C., and D. Durran, 2001: Three-Dimensional Effects in High-Drag-State Flows Over Long Ridges. *J. Atmos. Sci.*, **58**, 1051-1065.
- , C. C., and D. Durran, 2002: Lee Vortex Formation in Free-Slip Stratified Flow Over Ridges. Part II: Mechanisms of Vorticity and PV Production in Nonlinear Viscous Wakes. *J. Atmos. Sci.*, **59**, 1166-1181.

- , C. C., and R. Rotunno, 2005: The Dynamics of Orographic Wake Formation in Flows with Upstream Blocking. *J. Atmos. Sci.*, **62**, 3127-3150.
- Hirasaki, G. J., and J. D. Hellums, 1970: Boundary Conditions on the Vector and Scalar Potentials in Viscous 3-D Hydrodynamics. *Quart. J. Appl. Math*, **28**, 293-296.
- Hubert, L.F., and A.F. Krueger, 1962: Satellite Pictures of Mesoscale Eddies. *Mon. Wea. Rev.*, **90**, 457-463.
- Kundu, P.K., and I. M. Cohen, 2002: *Fluid Mechanics*, 3rd Edition. Academic Press, 700 pp.
- Oke, T. R., 1978: *Boundary Layer Climates*. Methuen, 372 pp.
- Peng, M. S., and W.T. Thompson, 2003: Some Aspects of the Effect of Surface Friction on Flows Over Mountains. *Quart. J. Roy. Meteor. Soc.*, **129**, 2527-2557.
- Rotunno, R., V. Grubišić, and P. K. Smolarkiewicz, 1999: Vorticity and Potential Vorticity in Mountain Wakes. *J. Atmos. Sci.*, **56**, 2796–2810.
- , R., and P.K. Smolarkiewicz, 1991: Further Results on Lee Vortices in Low-Froude-Number Flow. *J. Atmos. Sci.*, **48**, 2204-2211.
- Schär, C., and D. R. Durran, 1997: Vortex Formation and Shedding in Continuously Stratified Flows Past Isolated Topography. *J. Atmos. Sci.*, **54**, 534-554.
- , C., and R. B. Smith, 1993: Shallow-Water Flow Past Isolated Topography. Part I: Vorticity Production and Wake Formation. *J. Atmos. Sci.*, **50**, 1373-1400.
- , C., M. Sprenger, D. Lüthi, Q. Jiang, R. B. Smith, and R. Benoit, 2003: Structure and Dynamics of an Alpine Potential-Vorticity Banner. *Quart. J. Roy. Meteor. Soc.*, **189**, 825-856.

- Schneider, T., I.M. Held, and S.T. Garner, 2003: Boundary Effects in Potential Vorticity Dynamics. *J. Atmos. Sci.*, **60**, 1024-1040.
- Seki, M. P., J. J. Polovina, R. E. Brainard, R. R. Bidigare, C. L. Leonard, and D. G. Foley, 2001: Biological Enhancement at Cyclonic Eddies Tracked with GOES Thermal Imagery in Hawaiian Waters. *Geophys. Res. Lett.*, **28**, 1583– 1586.
- Smith, R.B., and V. Grubišić, 1993: Aerial Observations of Hawaii's Wake. *J. Atmos. Sci.*, **50**, 3728-3750.
- , R.B., and S. Grönas, 1993: Stagnation Points and Bifurcation in 3-D Mountain Airflow. *Tellus*, **45A**, 28-43.
- Smolarkiewicz, P.K., and R. Rotunno, 1989: Low Froude Number Flow Past Three-Dimensional Obstacles. Part I: Baroclinically Generated Lee Vortices. *J. Atmos. Sci.*, **46**, 1154-1164.
- Wilczak, J.M., and T.W. Christian, 1989: Case Study of an Orographically Induced Mesoscale Vortex (Denver Cyclone). *Mon. Wea. Rev.*, **118**, 1082-1102.

VITA

Jamie Brooke Smith received her Bachelor of Science degree in Atmospheric Science from the University of California at Davis in 2003, with a minor in Oceanography/Geology. She entered the Atmospheric Sciences program at Texas A&M University in September 2003, and she received her Master of Science degree in May 2006. Her research interests include both mountain wave dynamics and operational meteorology. On June 3, 2006, she will marry her college sweetheart Scott Meier in Los Angeles, California. Upon graduation, Ms. Smith will pursue a career in the National Weather Service as a general forecaster. Ms. Smith can be reached at the following address:

National Weather Service
Los Angeles/Oxnard Weather Forecast Office
520 North Elevar Street
Oxnard, CA 93030
Jamie.Meier@noaa.gov